The DOI for this manuscript is doi: 10.1175/2010JCLI3360.1

Optimal Tropical Sea Surface Temperature Forcing of North American Drought

Sang-Ik Shin,[1,2,*] Prashant D. Sardeshmukh,[1,2] Robert S. Webb[2]

[1] CIRES Climate Diagnostics Center, University of Colorado, Boulder, Colorado

[2] NOAA Earth System Research Laboratory, Boulder, Colorado

Journal of Climate

*Current affiliation: College of Marine Science, University of South Florida, St. Petersburg, Florida.

Corresponding author address: Dr. Sang-Ik Shin, University of South Florida, College of Marine Science, 140 7th Ave. S., St Petersburg, FL 33701.

E-mail: sangikshin@marine.usf.edu

ABSTRACT

The optimal anomalous sea surface temperature (SST) pattern for forcing North American drought is identified through atmospheric general circulation model integrations in which the response of the Palmer Drought Severity Index (PDSI) is determined for each of 43 prescribed localized SST anomaly "patches" in a regular array over the tropical oceans. The robustness and relevance of the optimal pattern are established through the consistency of results obtained using two different models, and also by the good correspondence of the projection time series of historical tropical SST anomaly fields on the optimal pattern with the time series of the simulated PDSI in separate model integrations with prescribed time-varying observed global SST fields for 1920-2005. It is noteworthy that this optimal drought forcing pattern differs markedly in the Pacific Ocean from the dominant SST pattern associated with the El Niño-Southern Oscillation (ENSO), and also shows a large sensitivity of North American drought to Indian and Atlantic Ocean SSTs.

1. Introduction

Droughts are among the costliest natural disasters associated with climate variations, costing $6- to $8-billion annually in global damages (Wilhite 2000; Trenberth et al. 2003). In response to increasing public concerns about future water availability, the climate research community is increasingly interested in understanding how global and regional hydrological cycles might be affected in a changing climate (IPCC 2007).

Many aspects of the North American hydroclimate are recognized to be sensitive to changes in tropical sea surface temperatures (SSTs), although which areas of the tropical oceans are most critical in this regard remains unclear. Some studies have highlighted the importance of a cooler eastern tropical Pacific Ocean in causing North American droughts at various times in Earth's history (e.g. the mid-Holocene, Shin et al. 2006; the Medieval Period, Seager et al. 2007a; the 1930s Dust Bowl, Schubert et al. 2004; and the current climate, Ting and Wang 1997), while others have also argued for a role of Indo-Pacific Warm Pool (Hoerling and Kumar 2003) and tropical North Atlantic (Schubert et al. 2004) SSTs. Recently, Schubert et al. (2009) intercompared the North American drought responses of five atmospheric general circulation models (GCMs) to three prescribed global SST patterns associated with observed SST variability: a multidecadal SST trend pattern, a pan-Pacific El Niño-Southern Oscillation (ENSO) pattern, and an Atlantic Multidecadal Oscillation (AMO) pattern. Despite some differences of detail among the model results, Schubert et al. (2009) were able to conclude that a cold Pacific in concert with a warm Atlantic is particularly effective at reducing precipitation over the continental U.S.

In this study, we used observations and two atmospheric GCMs to estimate the sensitivity of North American drought to SST changes at regularly spaced locations throughout the tropical oceans. A map of such sensitivities may also be interpreted as the "optimal" tropical SST forcing pattern of North American drought. The GCMs used were the National Center for Atmospheric Research (NCAR) atmospheric GCM CCM3 (Kiehl et al. 1998) and the Max Planck Institute for Meteorology (MPIM) atmospheric GCM ECHAM5 (Roeckner et al. 2003). As a measure of drought, we employed the widely used Palmer Drought Severity Index (PDSI; Palmer 1965), which is based on a supply-and-demand model of soil moisture. The PDSI at a particular location and time (Z_n) is related to that in the previous month (Z_{n-1}) as $Z_n = 0.897\, Z_{n\text{-}1} + 0.33\, K\, D_n$, where K is Palmer's "climate characteristic" at the location and D_n is the local precipitation supply relative to the expected precipitation needed to maintain a "normal" soil moisture level, which is a specified function of local surface air temperature, precipitation, and water holding capacity of the soil. The PDSI has been extensively used in drought monitoring and research, from weekly (e.g., the NOAA Drought Monitoring site[1]) to centennial (Dai et al. 1998; Dai et al. 2004; Wells et al. 2004) to millennial (Cook et al. 2004) time scales.

To estimate the PDSI from observations, we used three long-term surface air temperature and three precipitation datasets over land: the UEA CRU (Mitchell and Jones 2005), GISTEMP (Hansen et al. 2001), and MLASST (Smith and Raynolds 2005) datasets for surface air temperature; and the UEA CRU (Mitchell and Jones 2005), GPCC (Rudolf et al. 2005) and NOAA NCEP (Chen et al. 2002) datasets for precipitation. We also used the near-surface (2-

[1] www.cpc.noaa.gov/products/monitoring_and_data/drought.shtml

meter) air temperature and precipitation values from a 16-member ensemble of NCAR-CCM3 simulations (Seager et al. 2005; Seager 2007b; hereafter GOGA), and from another 24-member ensemble of MPIM-ECHAM5 simulations (Roeckner et al. 2006), both generated using prescribed time-varying observed global SSTs over the last century as boundary conditions[2]. The model resolution in both sets of simulations was T42 (~2.8° in longitude and latitude). Unless stated otherwise, all surface observational datasets used were also interpolated to this common T42 grid. The time series of the observed monthly PDSI were estimated using all 9 possible combinations of temperature and precipitation in the observational datasets, specifying water holding capacities compiled by Webb et al. (1993), and calibrating the PDSI model over the period 1961-2000.

A map of the average PDSI anomalies over North America during July 1998 - June 2002, a 4-yr period of widespread drought, is shown in Fig. 1 alongside a map of concurrent tropical SST anomalies, both computed relative to their 1961-2000 averages. The PDSI map represents an unweighted average of the 9 separate observational PDSI computations. The SST anomaly map was derived using the HadISST dataset (Rayner et al. 2003) at 1°×1° resolution. It shows a significantly cooler than normal tropical eastern Pacific, a warmer Indo-Pacific warm Pool, and a warmer tropical North Atlantic Ocean. Each of these features was argued in previous studies to be important in forcing this drought episode. However, the question of which particular feature, or combination of features, might have been most influential in this regard was not fully addressed.

[2] These model datasets are available at the data library of the International Research Institute for Climate and Society (IRI). The NCAR-CCM3 and MPIM-ECHAM5 simulations used here were available for 1856-2007 and 1950-2004, respectively.

In this study, we took both statistical and dynamical approaches to identify the optimal tropical SST forcing pattern of North American drought. The statistical approach was based on linear regressions. In the dynamical approach, we analyzed our own NCAR-CCM3 and MPIM-ECHAM5 simulations with idealized, steady, and localized SST anomaly "patches" imposed at 43 regularly spaced tropical locations on the climatological SST annual cycle. The locations and structures of these SST patches are shown in Fig. 1b. At each location, the magnitude of the prescribed area-averaged SST anomaly over the patch was 0.66 °C. For each patch in the Indo-Pacific domain, 16-member ensemble integrations were performed for 18 months starting October 1, for both warm (+0.66 °C) and cold (–0.66 °C) SST forcing. To obtain comparable signal-to-noise ratios for the smaller Atlantic patches, we performed 20-member ensemble integrations for 25 months for those patches [see Barsugli et al. (2006) for details of the experimental design]. We examine here only the linear PDSI response to each patch, defined as one-half of the difference between the ensemble-mean PDSI responses obtained for warm and cold patch forcing.

2. Optimal Forcing

As explained in Barsugli and Sardeshmukh (2002) and Barsugli et al. (2006), our patch experiments may be regarded as estimating a "Fuzzy Green's Function" of the global climate response to tropical SST anomalies, of which the PDSI response over North America represents only a part. Specifically, given our array of M (= 43) patches, and representing any tropical SST anomaly field as an M-component vector $\mathbf{T}'\delta A$ whose components denote the SST anomalies at the patch locations, the scalar area-averaged PDSI response $Z^{\Re}$ over North America to $\mathbf{T}'\delta A$

may be expressed as

$$Z^{\Re} = \mathbf{s}^{\mathrm{T}}\mathbf{T}'\delta A + \varepsilon ,$$

where **s** is an M-component sensitivity vector of the same dimension as $\mathbf{T}'\delta A$. The scalar ε represents error due to the linear approximation plus sampling noise, that we treated as an SST-independent Gaussian random variable in previous studies (Barsugli and Sardeshmukh 2002; Barsugli et al. 2006; Shin et al. 2006) and minimized by applying a smoothing spline procedure (Gu 1989). The sensitivity vector may also be regarded as an optimal SST forcing pattern for $Z^{\Re}$, in the sense that among all possible SST forcing patterns $\mathbf{T}'\delta A$ of the same r.m.s. magnitude over the tropics, $\mathbf{T}'\delta A = \mathbf{s}$ gives the maximum response in $Z^{\Re}$.

The sensitivity vector **s** was also estimated directly from observations and the GOGA simulations with prescribed observed SSTs, by linearly regressing the observed and simulated PDSI time series on the observed tropical SST anomaly fields. In this approach, the N-month time series of the area-averaged PDSI, represented by an N-component row vector **z**, was related to the N-month time series of the tropical SST anomaly fields, represented by an M×N matrix $\mathbf{T}'\delta A$, as

$$\mathbf{z} = \mathbf{a}^{\mathrm{T}}\mathbf{T}'\delta A + \mathbf{e}$$

where **a** is again an M-component sensitivity (i.e., optimal forcing) vector, and **e** is an N-

component error vector that is minimized in a least squares sense by the regression analysis. To perform clean comparisons of these regression-based sensitivities with those derived from the patch experiments, we coarse-grained the observed tropical SST anomaly fields to patch scales before performing the regression analyses[3] (Note that the SST anomaly fields in the GOGA simulations were the same as observed, by prescription). Because of our use of spatially non-orthogonal patch patterns [whose rationale is discussed in Barsugli and Sardeshmukh (2002)], we determined the appropriate observed tropical SST anomaly over the *j*-th patch, after accounting for geometric overlap factors, as $\ddot{T}_j'(t)\,\delta A_j = 4\beta_j \delta A_j$, where overhat denotes a weighted patch-area average and $4\beta_j$ is the weighted SST-anomaly average[4] over the patch. The factor 4 accounts for the fact that the sum of all our patches gives a spatially uniform 4°C anomaly over the tropics.

The dynamical and regression approaches are formally equivalent ($\mathbf{s} \approx \mathbf{a}$) under a linear approximation. In practice, however, one expects to obtain different results due to the limitation to finite ensemble sizes in the dynamical approach and the limited length of the observational SST record in the regression approach. It is therefore not clear, *a priori*, which of these methods yields a more accurate sensitivity pattern. We are, of course, also interested in what the pattern actually looks like.

---

[3] That is, we focused on the impact of observed SST anomalies on scales equal to or larger than the patch scales (see Fig. 1b).

[4] $\beta_j = \dfrac{\sum_k T'(x_k,t)\,T_j'(x_k)}{2\alpha \sum_k T_j'(x_k)}$, where $T'(x_k,t)$ is the time series of the observed topical SST anomaly, $T_j'(x_k)$ is the *j*-th patch pattern on grid x_k as shown in Fig. 1b, and α (~1.25) is the mean overlap factor, as explained in Barsugli et al. (2006).

3. Results

Figure 2 shows the optimal SST forcing pattern of annual area-averaged North American PDSI deduced from the regression analysis of the observations (upper panel) and GOGA simulations (lower panel) of the period 1961-2000. Note that the result in Fig. 2b represents an unweighted average of 16 separate optimal patterns estimated using the 16 individual GOGA simulations, as opposed to a pattern obtained from the ensemble-mean simulation (which is shown later in Fig. 3a). Although these sensitivity patterns are not directly comparable to maps of actual SST anomalies during any particular drought episode, it is nevertheless interesting to see some similarities between Fig. 2a and the actual mean SST anomaly pattern during the 1998-2002 drought (Fig. 1b), such as cooling over the east Pacific and warming over the west Pacific and north Atlantic Oceans. To that extent, the SST anomalies during 1998-2002 represented a "perfect ocean for drought" (Hoerling and Kumar 2003). Note however that over the Indian Ocean the signs of the sensitivity and actual anomalies were opposite during this period.

Given the chaotic nature of the climate system, one would expect sampling uncertainty to corrupt our estimated sensitivities even if the deterministic SST-forced dynamics were linear. The GOGA simulations provide one way to assess this uncertainty, using the spread of the sensitivities estimated from the 16 individual simulations. The hatched regions in Fig. 2b highlight the areas of large uncertainty obtained by this method. Indeed in these areas the estimated sensitivities are not statistically different from zero at the 90% level. In other areas, such as the Indian and eastern Pacific Oceans, the sensitivities are apparently more robust.

The GOGA simulations provide a cleaner way than the observations to estimate the sensitivity of only the SST-forced portion of the PDSI, by identifying that portion with the ensemble-mean PDSI in the 16 simulations. Performing the regression analysis on the ensemble-mean PDSI time series (which reduces the noise by a factor of 4) yields the optimal forcing pattern shown in Fig. 3a. Note that it is nearly identical to the pattern in Fig. 2b, except that the magnitudes are larger. This is because the air temperature and precipitation responses over the PDSI region are negatively correlated (warm and dry for droughts, cold and wet for wet spells). Also, with a much improved signal-to-noise ratio, all the major features of this sensitivity pattern are now statistically different from zero at the 90% level.

Figure 3b shows the map of PDSI sensitivities to tropical SSTs obtained by the dynamical approach, using our NCAR-CCM3 patch integrations. Bearing in mind that the PDSI, $Z = \mathbb{Z}\left(T, P\right)$, is a nonlinear function $\mathbb{Z}$ (Palmer's PDSI model) of surface air temperature T and precipitation P, the PDSI response in the years 1961-2000 to the *j*-th patch was determined by subtracting $\mathbb{Z}\left(\left\langle T\right\rangle, \left\langle P\right\rangle\right)$, calculated using the ensemble-mean $\left\langle T\right\rangle$ and $\left\langle P\right\rangle$ in the GOGA runs, from the Z calculated using the ensemble-mean GOGA $\left\langle T\right\rangle$ and $\left\langle P\right\rangle$ plus the $\left\langle T_j^{\Re}\right\rangle$ and $\left\langle P_j^{\Re}\right\rangle$ linear responses obtained in the patch integrations, i.e. $Z_j^{\Re} = \mathbb{Z}\left(\left\langle T\right\rangle + \left\langle T_j^{\Re}\right\rangle, \left\langle P\right\rangle + \left\langle P_j^{\Re}\right\rangle\right) - \mathbb{Z}\left(\left\langle T\right\rangle, \left\langle P\right\rangle\right)$. Averaging these PDSI responses to the patch over all years in the period 1961-2000, we defined the PDSI sensitivity to the *j*-th patch as the average PDSI response to a unit SST forcing in the patch, i.e. $S_j = \overline{Z_j^{\Re}} \left\{ \sum_k T_j'\left(x_k\right) \mathrm{d}A_k \right\}^{-1}$. These

raw sensitivity estimates were then assigned to the geographical centers of the patches (see Fig. 1b), and finally, spatially smoothed using a signal-to-noise ratio based smoothing spline procedure [as in Barsugli et al. (2006)] to produce the map shown in Fig. 3b.

Although the dynamically-derived PDSI sensitivities in Fig. 3b agree with the regression-based sensitivities in Fig. 3a in several important respects, such as showing sensitivity to cold SSTs in the tropical Pacific and Atlantic Oceans and to warm SSTs in the Gulf of Mexico, they differ in other important respects, especially in magnitude, and in some areas such as the northern edge of the Indo-Pacific Warm Pool, even in sign[5]. This raises a question as to which of these sensitivity maps is more accurate.

To answer this question, we projected the annually averaged tropical SST anomaly fields in the years 1920-2005 on the sensitivity patterns in Figs. 3a and 3b, and obtained the gray and green time series in Fig. 3c, respectively, as the SST-forced North American PDSI in the two cases. We then compared these *linearly reconstructed* PDSI responses using only the *tropical* SSTs with the ensemble-mean PDSI responses obtained in the fully *nonlinear* GOGA runs using *globally* prescribed SSTs over the period, indicated by the thick red curve. As an alternative reconstruction, we also estimated the PDSI response in each year as a weighted sum of the responses obtained for each patch, weighted by the observed SST anomaly in that year over that patch. These estimates are shown as the blue filled circles in Fig 3c. The only reason they deviate

[5] As noted in Seager (2007b), a cold Indian Ocean often occurs in conjunction with cold Pacific La Niña SSTs during a North American drought episode. This was, however, not true during the drought of 1998-2002, as shown in Fig 1b. The warm Indian ocean during that drought were nevertheless argued by Hoerling and Kumar (2003) to be important in forcing the drought, more consistent with the sensitivity in Fig 3b than in Fig.3a.

from the green curve is because they are derived from the raw responses to the patches, whereas the green curve is derived using the spatially smoothed sensitivities.

In the training period (1961-2000), both the regression and patch-based PDSI reconstructions are highly correlated with the GOGA responses (0.69 for the regression-based, and 0.80 and 0.83, respectively for the smoothed and raw patch-based reconstructions). Over the full period (1920-2005), however, the correlation of the regression-based reconstructions with the GOGA responses drops to 0.34, whereas the correlation of the patch-based reconstructions using the smoothed sensitivities remains high at 0.75. It is reassuring that the latter is slightly better than the correlation of 0.71 obtained using the noisier raw sensitivities, which might be expected to give slightly better results in the training period (because of fitting, in effect, not just the signal but also some of the noise) but worse results in an independent period. Overall, we conclude from this reconstruction test that the smoothed patch-based sensitivities of the North American PDSI to tropical SSTs (Fig. 3b) are more accurate than the sensitivities derived from regressing the ensemble-mean PDSI time series in the GOGA runs on the tropical SSTs (Fig. 3a).

We have further confirmed the robustness of the patch-based sensitivity map in Fig. 3b by repeating the entire patch experiment with a different model, the MPIM-ECHAM5 atmospheric GCM, and following identical sensitivity map construction procedures as for the NCAR-CCM3 model. The smoothed sensitivity map derived from the MPIM-ECHAM5 model is shown in Fig. 4. It is very similar to the map in Fig. 3b; the pattern correlation is 0.68. Among the reassuring similarities are the large sensitivity of North American drought to SST anomalies in the *off-equatorial* eastern Pacific (*north* of the Niño-3 region) and in the Gulf of Mexico/Caribbean Sea.

Having established the robustness of the optimal SST forcing pattern for maximizing the drought response over North America, it is of interest to clarify how different portions of that pattern contribute to the maximal response. To this end we present in Fig. 5 maps of the linearly reconstructed 200 hPa geopotential height and surface precipitation responses to the Indian, Pacific, and Atlantic Ocean portions of the optimal SST forcing field with a 1 °C r.m.s. amplitude over the tropical oceans. Following a procedure similar to the linear reconstruction of the PDSI responses in Fig. 3c, the reconstructed responses in Fig. 5 were determined as weighted sums of the responses to the individual patches, with weights proportional to the magnitude of the optimal SST forcing field at the patch locations.

The precipitation response to the Pacific portion of the optimal SST forcing (Fig. 5b) has a structure similar to that associated with La Niña events: negative anomalies along the SST anomaly minimum flanked by positive anomalies [see, e.g., Fig. 5 of Schubert et al. (2009)]. The upper tropospheric geopotential height response shows a familiar wave train dispersing from the tropics in response to the eastern tropical Pacific diabatic heating anomalies associated with the precipitation anomalies (e.g. Ting and Sardeshmukh 1993), producing a ridge over the continental U.S. and sustaining drought conditions there. The response to the Indian Ocean forcing (Fig. 5a), although considerably weaker, reinforces the response over the U.S. to the Pacific forcing by also generating an upper tropospheric ridge. The tropical Atlantic forcing generates an even stronger upper tropospheric ridge over the U.S. than the Pacific forcing, primarily in response to the SST forcing in the Gulf of Mexico/Caribbean Sea area. The upper level ridge response is associated with a low level trough response, with the accompanying low

level cyclonic wind anomalies reducing the moisture supply from the Gulf of Mexico/Caribbean Sea to the Great Plains (figure not shown) and sustaining drought conditions there as shown in previous studies (e.g., Shin et al. 2006; Wang et al. 2006).

Before closing this section, we note that one concern one may have with our sensitivity analysis is that we have characterized North American drought in terms of a single number, the area-averaged PDSI. As is well known, there are large differences in drought occurrence and characteristics, for instance, over the western and eastern parts of the U.S. This raises the issue of whether the optimal SST forcing patterns for regional U.S. droughts are substantially different from the optimal forcing pattern for the continental-scale drought discussed thus far. The fact that the response patterns in Fig. 5 are spatially coherent over much of the U.S suggests otherwise. Still, for additional confirmation, we repeated our entire PDSI sensitivity analysis for 5 sub-continental regions (Fig. 6) using the NCAR-CCM3 patch integrations. The resulting optimal SST patterns for maximizing the PDSI in each of these regions are shown in Fig. 6. As expected, they are broadly similar to one another and also to the optimal SST pattern in Fig. 3b for North America as a whole. In particular, despite differences of detail, they all indicate strong drought sensitivity to a cold tropical Pacific Ocean and a warm Gulf of Mexico/Caribbean sea. The sensitivity to a warm north Indian and northwestern tropical Pacific Ocean also appears to be robust. Chief among the differences is the very different sensitivity of Mexican drought to SSTs in the Gulf of Mexico/Caribbean sea area.

Finally, to assess the robustness of these regional drought sensitivities, we repeated for each of the 5 regions the entire analysis of Fig. 3c of comparing the linearly reconstructed PDSI time

series with the corresponding ensemble-mean PDSI time series in the NCAR-CCM3 GOGA simulations. As in Fig. 3c, the linearly reconstructed time series were obtained by projecting the annually averaged observed tropical SST anomaly fields in 1920-2005 on each of the sensitivity maps in Fig. 6, and also on the corresponding regression-based sensitivity maps (not shown). The correlations of these regional patch-based and regression-based linearly reconstructed PDSI time series with the ensemble-mean GOGA time series are summarized in Table 1. They provide further confirmation that the smoothed patch-based sensitivity maps are more accurate than the regression-based maps.

4. Summary and Conclusions

In this study, we estimated the sensitivity of a widely used index of drought over North America, the PDSI, to SST changes at regularly spaced locations over the tropical oceans. Plotting the PDSI sensitivities at those tropical locations yields a sensitivity map that can also be interpreted as an optimal SST anomaly pattern for maximizing drought over North America, i.e. as an objectively determined "perfect ocean" for North American drought. Another equally important interpretation of such a sensitivity map is that it represents the Green's Function of PDSI responses to tropical SST forcing, enabling the PDSI response to an arbitrary tropical SST anomaly field to be estimated as simply the projection of that anomaly field on the sensitivity pattern. We demonstrated the utility of this latter interpretation by "reconstructing" the annual PDSI responses to observed tropical SST changes over 1920-2005 through such projections, and showing that this reconstructed PDSI response time series correlated quite highly (0.75) with the ensemble-mean PDSI response time series obtained in an ensemble of NCAR-CCM3 runs for 1920-2005 with prescribed observed global SSTs (i.e., the GOGA simulations).

We derived our sensitivity map by determining the PDSI responses to localized SST anomaly "patches" prescribed at 43 regularly spaced locations over the tropical oceans. We did this using two different atmospheric GCMs, the NCAR-CCM3 and the MPIM-ECHAM5 models, and obtained generally similar results (Fig. 3b and Fig. 4).

We argued that the sensitivity map obtained through this dynamical "forward" Green's Function approach was superior to that obtained from regressing the PDSI on tropical SSTs in observations or in GCM simulations of the past century with prescribed observed SSTs (GOGA runs), even though the approaches are formally similar. The main reason for this superiority, we suspect, may be that an ensemble of anomaly-patch integrations with a relatively large 0.66 °C prescribed SST forcing is better able to determine the response to SST changes in areas of relatively weak observed SST variability, which is more difficult to estimate from observations or GOGA runs because of the relatively small signal-to-noise ratio.

It should be stressed that the values in Fig. 3b, Fig. 4, and Fig. 6 are measures of the *sensitivity* of the PDSI to tropical SSTs, and not measures of the *association* of the PDSI and tropical SSTs. Sensitivity is not correlation, even though it can be approximately deduced from correlations. One should not be surprised that our sensitivity patterns look different from the La Niña SST pattern often associated with North American drought, or from a pattern obtained by correlating the PDSI with tropical SSTs, or from patterns obtained through combined-EOF or SVD analyses of the PDSI and tropical SSTs. These latter patterns are patterns of association, whose relevance

to drought arises basically from their positive (but imperfect) spatial correlation with our sensitivity patterns.

It is also important to distinguish between the *sensitivity* of drought to an SST anomaly at a tropical location and the *actual impact* on the drought of that SST anomaly, which is the sensitivity multiplied by the SST anomaly. Regions of large sensitivity need not coincide with those of large impact. For example, as Figs. 3b and 4 show, the eastern equatorial Pacific is only one of several tropical regions to which North American drought is sensitive, but because it is also a region of large ENSO-related interannual SST variability, it has a relatively large actual impact on North American drought on interannual scales than, say, the Indian Ocean. On longer time scales, the situation could be different, with a warming trend of the Indian Ocean possibly having a larger impact on North American drought trends.

Finally, interpreting the sensitivity maps in Figs. 3b, 4, and 6 as Green's Functions raises the exciting possibility of using them to generate forecasts of the PDSI in a "two-tiered" prediction system, in which a tropical SST forecast generated by other means is simply projected on such sensitivity patterns, possibly derived from a number of other GCMs in addition to the two GCMs discussed here. One could use such an approach to generate PDSI projections several seasons to several decades ahead. This is a topic of current research.

Acknowledgments. We are grateful to Dr. J. Barsugli for his contributions in earlier phases of this work. We thank Drs. M. Hoerling, K. Mo, and D. Legler for discussions at the Drought in Coupled Models Project (DRICOMP) Workshop that were helpful in preparing the manuscript.

We also thank J. Eischeid and Dr. A. Dai for sharing the PDSI model code used in this study. The Max Planck Institute for Meteorology kindly provided the ECHAM5 model used here. All our simulations were performed at the NOAA ESRL High Performance Computing Systems (HPCS) facility. This research was funded by NSF, NOAA, NASA, and DOE as a DRICOMP grant under the U.S. CLIVAR Program (www.usclivar.org).

REFERENCES

Barsugli, J. J., and P. D. Sardeshmukh, 2002: Global atmospheric sensitivity to tropical SST anomalies throughout the Indo-Pacific basin. *J. Climate*, **15**, 3427-3442.

Barsugli, J. J., S.-I. Shin, and P. D. Sardeshmukh, 2006: Sensitivity of global warming to the pattern of tropical ocean warming. *Climate Dyn.*, **27**, 483-492.

Chen, M., P. Xie, J. E. Janowiak, and P. A. Arkin, 2002: Global land precipitation: A 50-yr monthly analysis based on gauge observations. *J. Hydrometeor.*, **3**, 249-266.

Cook, E. R., C. A. Woodhouse, C. M. Eakin, D. M. Meko, and D. W. Stahle, 2004: Long-Term Aridity Changes in the Western United States. *Science*, **306**, 1015-1018.

Dai, A., K. E. Trenberth, and T. R. Karl, 1998: Global variations in droughts and wet spells. *Geophys. Res. Lett.*, **17**, 3367-3370.

Dai, A., K. E. Trenberth, and T. Qian, 2004: A global dataset of Palmer Drought Severity Index for 1870-2002: relationship with soil moisture and effects of surface warming. *J. Hydrometeor.*, **5**, 1117-1130.

Gu, C., 1989: RKPACK and its applications: Fitting smoothing spline models. *Proceedings of the Statistical Computing Section*, American Statistical Society, 42-51.

Hansen, J. E., and Coauthors, 2001: A closer look at United States and global surface temperature change. *J. Geophys. Res.*, **106**, 23947-23963.

Hoerling, M. and A. Kumar, 2003: The perfect ocean for drought. *Science*, **299**, 691-694.

IPCC, 2007: Climate Change 2007: The Physical Science Basis. Contribution of Working Group I to the Fourth Assessment Report of the Intergovernmental Panel on Climate Change [Solomon, S., D. Qin, M. Manning, Z. Chen, M. Marquis, K. B. Averyt, M. Tignor, and H. L. Miller (eds.)]. Cambridge University Press, Cambridge, United Kingdom and New

York, pp. 996.

Kiehl, J. T., J. J. Hack, G. B. Bonan, B. A. Bovile, D. A. Williamson, and P. J. Rasch, 1998: The National Center for Atmospheric Research Community Climate Model: CCM3. *J. Climate*, **11**, 1131-1178.

Mitchell, T. D., and P. D. Jones, 2005: An improved method of constructing a database of monthly climate observations and associated high-resolution grids. *Int. J. Climatol.*, **25**, 693-712.

Palmer, W. C., 1965: Meteorological drought. Research Paper 45, U.S. Dept. of Commerce, 58 pp.

Rayner, N. A., D. E. Parker, E. B. Horton, C. K. Folland, L. V. Alexander, D. P. Powell, E. C. Kent, and A. Kaplan, 2003: Global analyses of sea surface temperature, sea ice, and night marine air temperature since the late nineteenth century. *J. Geophys. Res.*, **108**, 4407-4443.

Roeckner, E., and Coauthors, 2003: The atmospheric general circulation model ECHAM5. Part I: Model description. Max-Planck Institute for Meteorology Rep. 349, 127pp.

Roeckner, E., and Coauthors, 2006: Sensitivity of simulated climate to horizontal and vertical resolution in the ECHAM5 atmosphere model. *J. Climate*, **19**, 3771-3791.

Rudolf, B., C. Beck, J. Grieser, and U. Schneider, 2005: Global precipitation analysis products. Global Precipitation Climatology Centre (GPCC), DWD, Internet Publication, 1-8.

Schubert, S. D., M. J. Suarez, P. J. Region, R. D. Koster, and J. T. Bacmeister, 2004: On the cause of the 1930s Dust Bowl. *Science*, **303**, 1855-1859.

Schubert, S. D., and Coauthors, 2009: A U.S. CLIVAR project to assess and compare the responses of global climate models to drought-related SST forcing patterns: overview and

results. *J. Climate*, **22**, 5251-5272.

Seager, R., Y. Kushnir, C. Herweijer, N. Naik and J. Velez(Nakamura), 2005: Modeling of tropical forcing of persistent droughts and pluvials over western North America: 1856-2000. *J. Climate*, **18**, 4065-4088.

Seager, R., N. Graham, C. Herweijer, A. L. Gordon, Y. Kushnir and E. Cook, 2007a: Blueprints for Medieval hydroclimate. *Quat. Sci. Rev.*, **26**, 2322-2336.

Seager, R., 2007b: The Turn of the Century drought across North America: Global context, dynamics and past analogues, *J. Climate*, **20**, 5527-5552.

Shin, S., P. D. Sardeshmukh, R. S. Webb, R. J. Oglesby, J. J. Barsugli, 2006: Understanding the mid-Holocene Climate. *J. Climate*, **19**, 2801-2817.

Smith, T. M., and R. W. Raynolds, 2005: A global merged land-air-sea surface temperature reconstruction based on historical observations (1880-1997). *J. Climate*, **18**, 2021-2036.

Ting M., and P. D. Sardeshmukh, 1993: Factors determining the extratropical response to equatorial diabatic heating anomalies. *J. Atmos. Sci.*, **50**, 907–918.

Ting, M.-F. and H. Wang, 1997: Summertime United States precipitation variability and its relation to Pacific sea surface temperatures. *J. Climate*, **10**, 1853-1873.

Trenberth, K. E., A. Dai, R. M. Rasmussen, and D. B. Parsons, 2003: The changing character of precipitation. *Bull. Amer. Meteor. Soc.*, **84**, 1205-1217.

Wang, C., D. B. Enfield, S.-K. Lee, and C. W. Landsea, 2006: Influences of the Atlantic warm pool on Western Hemisphere summer rainfall and Atlantic hurricanes. *J. Climate*, **19**, 3011-3028.

Webb, R. S., C. E. Rosenzwig, and E. R. Levine, 1993: Specifying land surface characteristics in general circulation models: Soil profile data set and derived water-holding capacities.

Global Biogeochem. Cycles, **7**, 97-108.

Wells, N., S. Goddard, and M.J. Hayes, 2004: A self-calibrating Palmer Drought Severity Index. *J. Climate*, **17**, 2335-2351.

Wilhite, D. A., 2000: Drought as a natural hazard: Concepts and definitions. *Droughts: A Global Assessment*, D. A. Wilhite, Ed., Routledge, 3-18.

Figure Captions

Fig. 1 Observed (**a**) PDSI and (**b**) SST anomalies averaged over the 4-year period July 1998-June 2002 relative to the 1961-2000 average. The PDSI values shown represent an unweighted average of 9 separate PDSI computations performed using all 9 combinations of three surface temperature and three precipitation observational datasets (see text for details). The SST anomalies are from the HadISST (Rayner et al. 2003) dataset. Our North American region of interest (land points only) is indicated in the upper panel by the black rectangle. The black dots in the lower panel represent the centers of the prescribed SST anomaly patches used to identify the optimal tropical SST forcing pattern of North American drought. The elliptical patterns of the imposed Indo-Pacific (*left*) and Atlantic (*right*) SST patches are shown in the gray shaded rectangles at the bottom of the figure.

Fig. 2 (**a**) Sensitivity of the North American PDSI to Tropical SSTs derived from linear regressions of the annually averaged observed PDSI anomalies on the annually averaged tropical SST anomalies during the period 1961-2000, in units of 10^{-2} Index $(10^6$ km^2 °C$)^{-1}$. Note that the observed tropical SST anomaly fields were truncated to the spatial resolution of the patches in Fig. 1 prior to performing the regression analysis. (**b)** The same as (a), but derived from linear regressions of the PDSI in the GOGA simulations on the observed SSTs. The GOGA regression analysis was done for each ensemble member separately; the plot shows an unweighted average of the 16 such sensitivity maps obtained. The hatched regions show where the average sensitivity is indistinguishable from zero at the 90% level.

Fig. 3 (a) Sensitivity of the North American PDSI to Tropical SSTs derived from linear regressions of the annually averaged *ensemble-mean* PDSI in the GOGA simulations on the observed SSTs during 1961-2000, in units of 10^{-2} Index $(10^6\ km^2\ °C)^{-1}$. (**b)** The same as (a), but derived from the NCAR-CCM3 patch integrations. (**c**) The annually averaged ensemble-mean PDSI in the GOGA simulations over the period 1920-2005 (thick red line), and the corresponding linearly reconstructed PDSI time series determined using the projection of the observed annually averaged SST anomaly fields on the regression-based sensitivity pattern shown in (a) (gray curve), and on the patch-experiment based sensitivity pattern shown in (b) (green curve). A third series of reconstructions, obtained as the weighted sum of the responses to the individual patches, with the weights proportional to the SST anomaly amplitude in each patch in each year, is indicated by the blue dots. See text for further details.

Fig. 4 The same sensitivity map as in Fig. 3b, but derived from identical patch integrations performed using the MPIM-ECHAM5 model.

Fig. 5 Optimal SST anomaly field (same pattern as in Fig. 3b) with root-mean-square amplitude of 1°C over the tropical oceans **(top panel)**. Linearly reconstructed precipitation (color shaded) and 200 hPa height (contoured) response fields to the Indian **(a),** Pacific **(b),** and Atlantic **(c)** basin portions of the optimal SST anomaly field. The basin boundaries are indicated by thick black lines in the top panel. The zero contour in the 200 hPa height response field is thickened and negative contours are dashed.

Fig. 6 Sensitivity of regionally averaged PDSI in 5 North American regions to Tropical SSTs, derived using the NCAR-CCM3 patch integrations, in units of 10^{-2} Index $(10^6\ km^2\ °C)^{-1}$. The 5 regions are indicated by five colored rectangles: (i) Central US (Blue; 32.5°N-50°N, 112.75°W-91°W), (ii) SW US (Black; 30°N-40°N, 125°W-102.5°W), (iii) N Mexico (Red; 20°N-27.5°N, 112.75°W-91°W), (iv) SE US (Green; 25.5°N-37.5°N, 107.5°W-77.5°W), and (v) NE US (Yellow; 35°N-45°N, 97.5°W-72.5°W).

Table 1 Correlations of the linearly reconstructed regional PDSI time series over 1920-2005 with the ensemble-mean regional PDSI time series obtained in the NCAR CCM3 GOGA simulations, for the 5 regions shown in Figure 6. Results are shown for reconstructed time series obtained by projecting the observed tropical SST anomaly fields for 1920-2005 on the regression-based, raw patch-based, and spatially smoothed patch-based (i.e., optimal) regional PDSI sensitivity maps. Numbers in parentheses indicate the correlations over the training period (1961-2000).

Region		Correlations of GOGA PDSI Responses with Reconstructed Responses		
		Regressions	Patch-Based Raw Sensitivites	Patch-Based Smoothed Sensitivites
(i)	Central US	0.29 (0.66)	0.65 (0.79)	0.72 (0.75)
(ii)	SW US	0.38 (0.65)	0.62 (0.74)	0.68 (0.75)
(iii)	N Mexico	0.64 (0.70)	0.82 (0.89)	0.76 (0.86)
(iv)	SE US	0.40 (0.71)	0.75 (0.86)	0.77 (0.86)
(v)	NE US	0.36 (0.62)	0.75 (0.86)	0.77 (0.89)

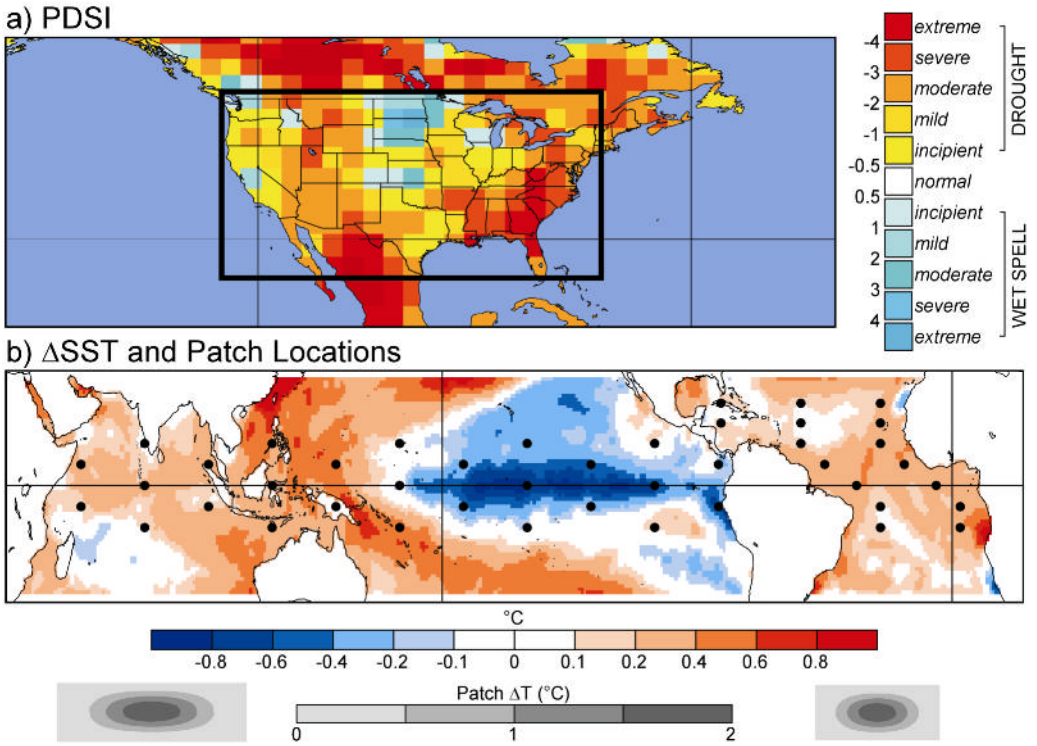

Fig. 1 Observed (**a**) PDSI and (**b**) SST anomalies averaged over the 4-year period July 1998-June 2002 relative to the 1961-2000 average. The PDSI values shown represent an unweighted average of 9 separate PDSI computations performed using all 9 combinations of three surface temperature and three precipitation observational datasets (see text for details). The SST anomalies are from the HadISST (Rayner et al. 2003) dataset. Our North American region of interest (land points only) is indicated in the upper panel by the black rectangle. The black dots in the lower panel represent the centers of the prescribed SST anomaly patches used to identify the optimal tropical SST forcing pattern of North American drought. The elliptical patterns of the imposed Indo-Pacific (*left*) and Atlantic (*right*) SST patches are shown in the gray shaded rectangles at the bottom of the figure.

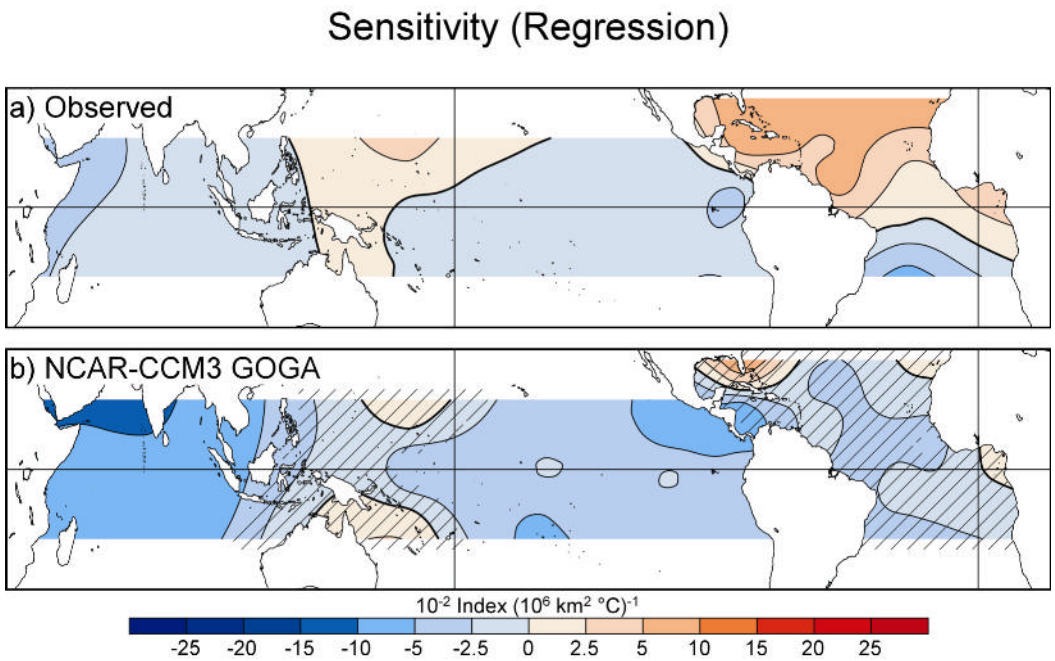

Fig. 2 (**a**) Sensitivity of the North American PDSI to Tropical SSTs derived from linear regressions of the annually averaged observed PDSI anomalies on the annually averaged tropical SST anomalies during the period 1961-2000, in units of 10^{-2} Index $(10^6$ km^2 °C$)^{-1}$. Note that the observed tropical SST anomaly fields were truncated to the spatial resolution of the patches in Fig. 1 prior to performing the regression analysis. (**b)** The same as (a), but derived from linear regressions of the PDSI in the GOGA simulations on the observed SSTs. The GOGA regression analysis was done for each ensemble member separately; the plot shows an unweighted average of the 16 such sensitivity maps obtained. The hatched regions show where the average sensitivity is indistinguishable from zero at the 90% level.

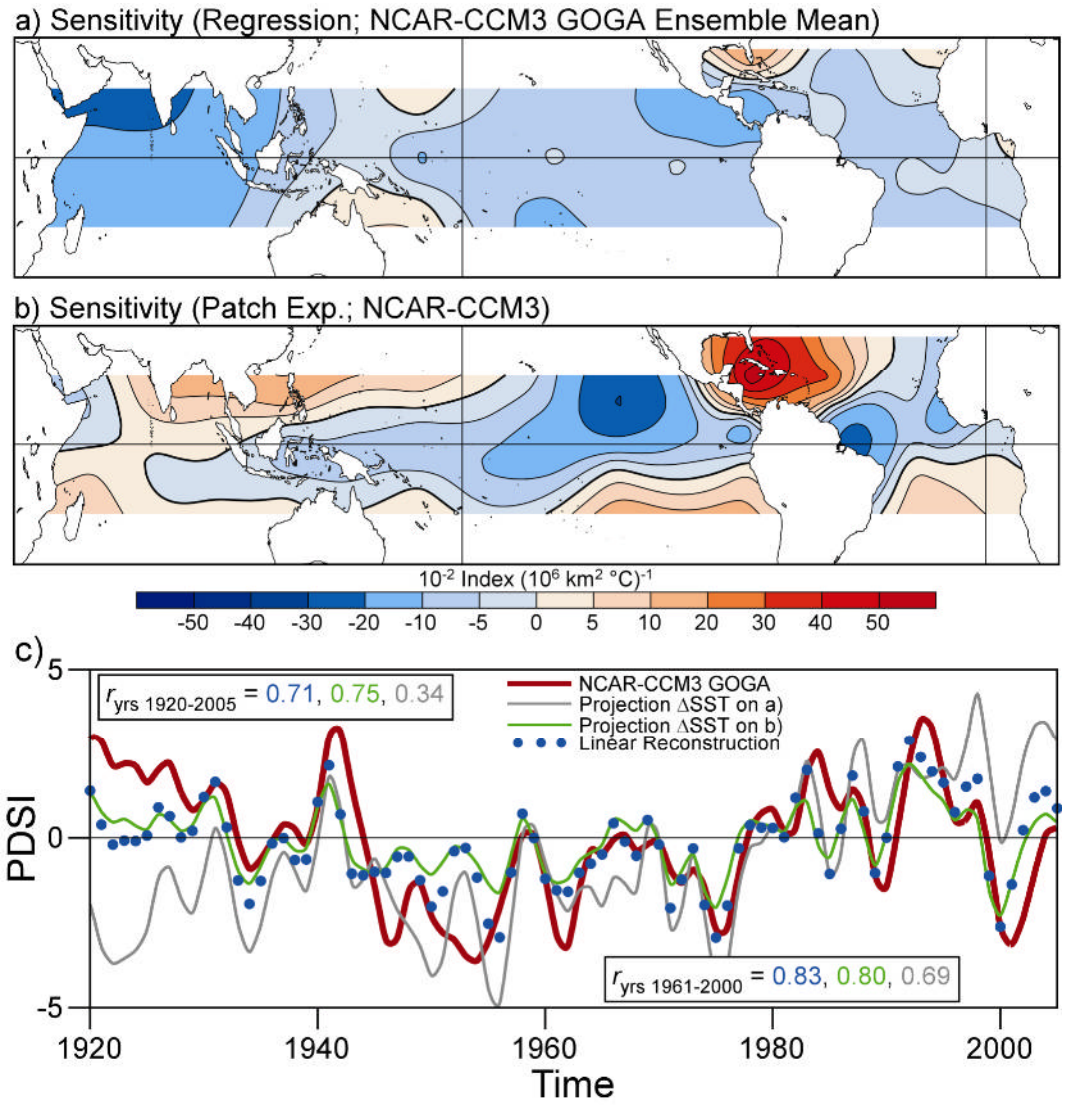

Fig. 3 (a) Sensitivity of the North American PDSI to Tropical SSTs derived from linear regressions of the annually averaged *ensemble-mean* PDSI in the GOGA simulations on the observed SSTs during 1961-2000, in units of 10^{-2} Index $(10^6$ km^2 °C$)^{-1}$. **(b)** The same as (a), but derived from the NCAR-CCM3 patch integrations. (**c**) The annually averaged ensemble-mean PDSI in the GOGA simulations over the period 1920-2005 (thick red line), and the corresponding linearly reconstructed PDSI time series determined using the projection of the observed annually averaged SST anomaly fields on the regression-based sensitivity pattern shown in (a) (gray curve), and on the patch-experiment based sensitivity pattern shown in (b) (green curve). A third series of reconstructions, obtained as the weighted sum of the responses to the individual patches, with the weights proportional to the SST anomaly amplitude in each patch in each year, is indicated by the blue dots. See text for further details.

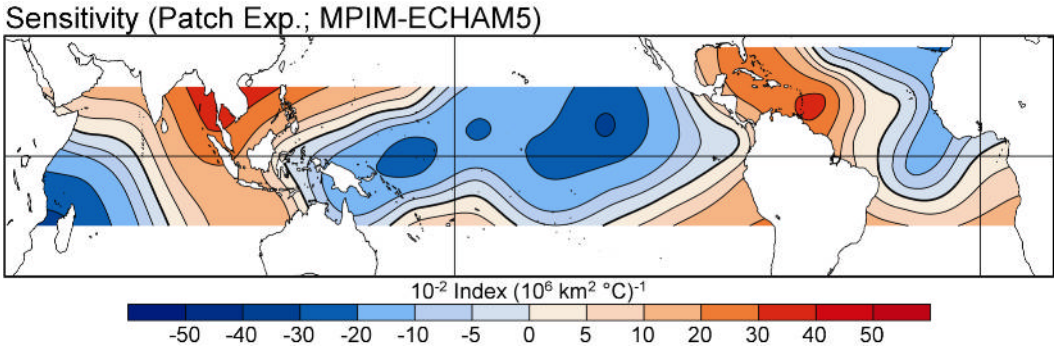

Fig. 4 The same sensitivity map as in Fig. 3b, but derived from identical patch integrations performed using the MPIM-ECHAM5 model.

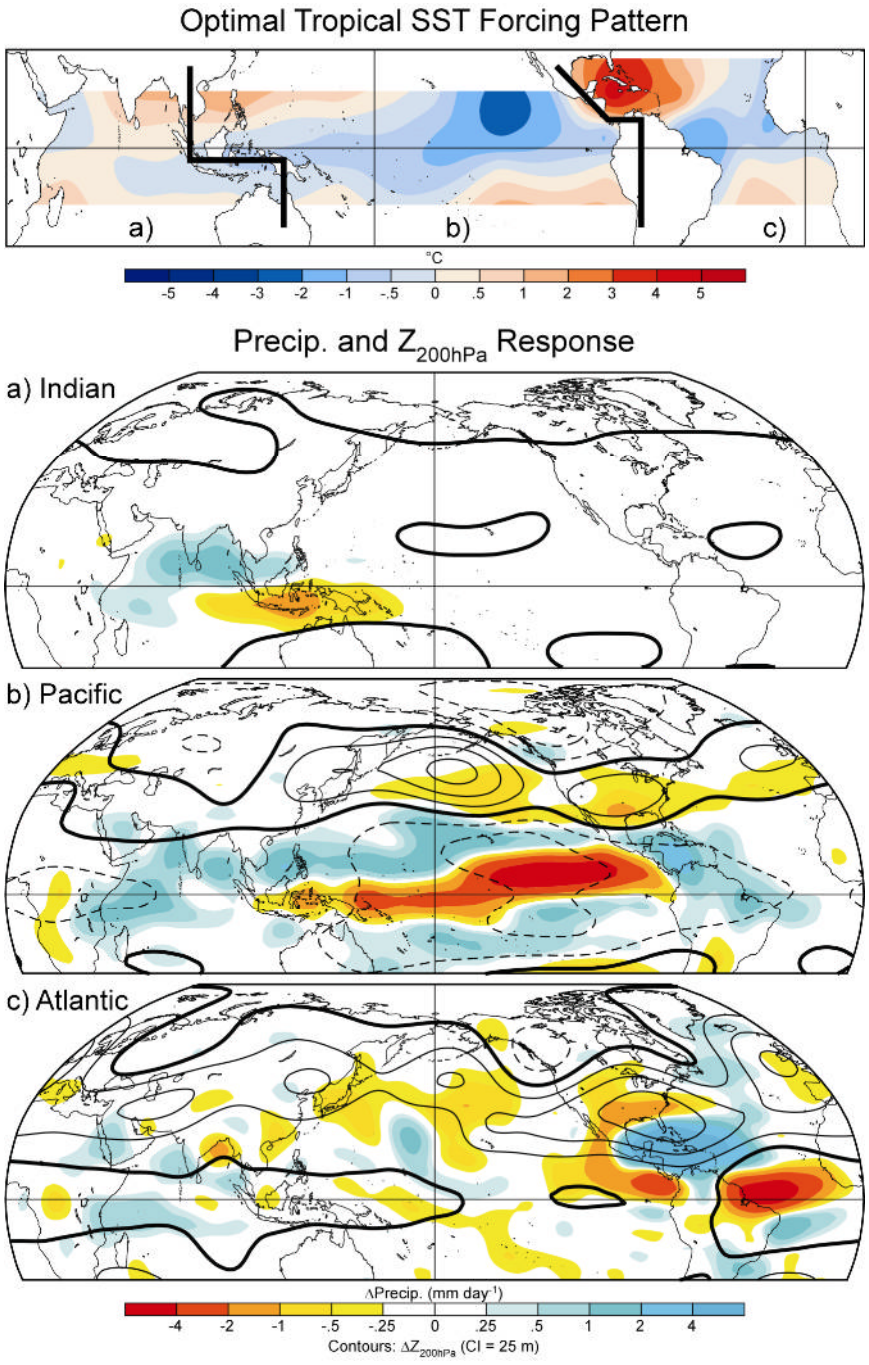

Fig. 5 Optimal SST anomaly field (same pattern as in Fig. 3b) with root-mean-square amplitude of 1°C over the tropical oceans **(top panel)**. Linearly reconstructed precipitation (color shaded) and 200 hPa height (contoured) response fields to the Indian **(a),** Pacific **(b),** and Atlantic **(c)** basin portions of the optimal SST anomaly field. The basin boundaries are indicated by thick black lines in the top panel. The zero contour in the 200 hPa height response field is thickened and negative contours are dashed.

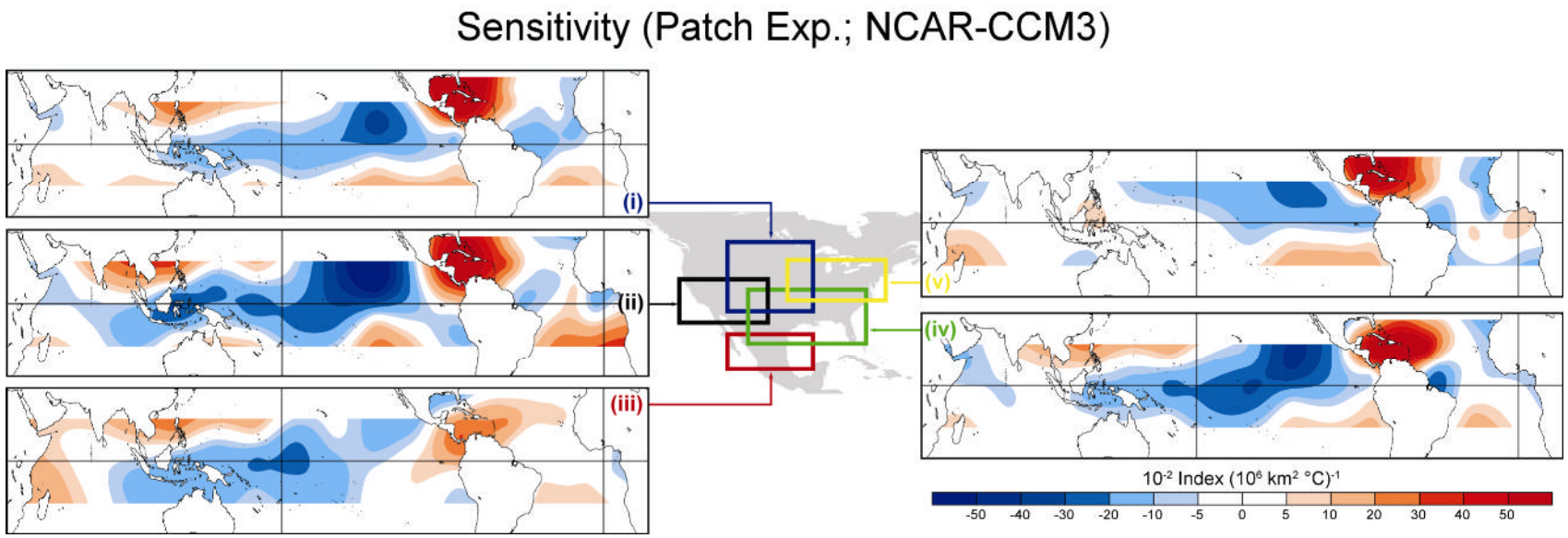

Fig. 6 Sensitivity of regionally averaged PDSI in 5 North American regions to Tropical SSTs, derived using the NCAR-CCM3 patch integrations, in units of 10^{-2} Index (10^{6} km^{2} °C)$^{-1}$. The 5 regions are indicated by five colored rectangles: (i) Central US (Blue; 32.5°N-50°N, 112.75°W-91°W), (ii) SW US (Black; 30°N-40°N, 125°W-102.5°W), (iii) N Mexico (Red; 20°N-27.5°N, 112.75°W-91°W), (iv) SE US (Green; 25.5°N-37.5°N, 107.5°W-77.5°W), and (v) NE US (Yellow; 35°N-45°N, 97.5°W-72.5°W).